

Article

# Nanostructured Cobalt Doped Barium Strontium Titanate Thin Films with Potential in CO<sub>2</sub> Detection

Cristina F. Ciobota <sup>1</sup>, Roxana M. Piticescu <sup>1</sup>, Ciprian Neagoe <sup>1</sup>, Ioan A. Tudor <sup>1</sup>, Alexandru Matei <sup>1</sup>, Dumitru V. Dragut <sup>1</sup>, Arcadie Sobetkii <sup>2</sup>, Elena M. Anghel <sup>3</sup>, Adelina Stanoiu <sup>4</sup>, Cristian E. Simion <sup>4</sup>, Ovidiu G. Florea <sup>4</sup> and Simona E. Bejan <sup>1,\*</sup>

<sup>1</sup> Laboratory of Advanced and Nanostructured Materials, National Research & Development Institute for Non-Ferrous and Rare Metals—IMNR, 102 Biruintei Blvd., 077145 Pantelimon, Romania; rusticristina@yahoo.com (C.F.C.); roxana.piticescu@imnr.ro (R.M.P.); ciprian.neagoe@imnr.ro (C.N.); atudor@imnr.ro (I.A.T.); alex.matei@imnr.ro (A.M.); dragutv@imnr.ro (D.V.D.)

<sup>2</sup> MGM Star Construct SRL, 7 Pancota Street, Building 13, 022773 Bucharest, Romania; office@mgmstar.ro

<sup>3</sup> Oxide Compounds and Materials Science Laboratory, “Ilie Murgulescu” Institute of Physical Chemistry of the Romanian Academy, 202 Splaiul Independentei, 060021 Bucharest, Romania; manghel@icf.ro

<sup>4</sup> Laboratory of Atomic Structures and Defects in Advanced Materials, National Institute of Materials Physics, Atomîștilor 405A, P.O. Box MG-7, 077125 Măgurele, Romania; adelina.stanoiu@infim.ro (A.S.); simion@infim.ro (C.E.S.); ovidiu.florea@infim.ro (O.G.F.)

\* Correspondence: sbejan@imnr.ro; Tel.: +40-21-352-2048

Received: 23 September 2020; Accepted: 21 October 2020; Published: 27 October 2020



**Abstract:** In this work, (Ba<sub>0.75</sub>Sr<sub>0.25</sub>)(Ti<sub>0.95</sub>Co<sub>0.05</sub>)O<sub>3</sub> perovskite nanostructured material, denoted subsequently as Co-doped BaSrTiO<sub>3</sub>, was synthesized in a one-step process in hydrothermal conditions. The obtained powder was heat-treated at 800 °C and 1000 °C, respectively, in order to study nanostructured powder behavior during thermal treatment. The Co-doped BaSrTiO<sub>3</sub> powder was pressed into pellets of 5.08 cm (2 inches) then used for thin film deposition onto commercial Al<sub>2</sub>O<sub>3</sub> substrates by RF sputtering method. The microstructural, thermal, and gas sensing properties were investigated. The electrical and thermodynamic characterization allowed the evaluation of thermodynamic stability and the correlation of structural features with the sensing properties revealed under real operating conditions. The sensing behavior with respect to the temperature range between 23 and 400 °C, for a fixed CO<sub>2</sub> concentration of 3000 ppm, highlighted specific differences between Co-doped BaSrTiO<sub>3</sub> treated at 800 °C compared to that treated at 1000 °C. The influence of the relative humidity level on the CO<sub>2</sub> concentrations and the other potential interfering gases was also analyzed. Two possible mechanisms for CO<sub>2</sub> interaction were then proposed. The simple and low-cost technology, together with the high sensitivity when operating at room temperature corresponding to low power consumption, suggests that Co-doped BaSrTiO<sub>3</sub> has a good potential for use in developing portable CO<sub>2</sub> detectors.

**Keywords:** hydrothermal synthesis; Co-doped BaSrTiO<sub>3</sub> perovskite nanopowders; RF sputtering method; Co-doped BaSrTiO<sub>3</sub> thin film; CO<sub>2</sub> detection

## 1. Introduction

Recent progress in manufacturing advanced materials and technologies has seen the development of novel sensorial thin films for the rapid detection of a wide range of environmentally-polluting industrial waste. Industrial gases containing CO, NO<sub>x</sub>, NH<sub>3</sub>, CH<sub>4</sub>, SO<sub>2</sub>, and CO<sub>2</sub>, as well as exhaust gases from automobiles, require special detection and monitoring sensors to avoid harm to humans and the surrounding atmosphere [1]. The notable increase in public health issues and climate threats requires huge efforts in order to reduce the impact of these dangerous gases. The development

of efficient monitoring and control of low-cost gas sensors could be the first step to address such a challenge.

Barium strontium titanate (BST,  $\text{Ba}_x\text{Sr}_{1-x}\text{TiO}_3$ ) is a material with a perovskite structure that has attracted the interest of researchers and engineers due to its ferroelectric properties and composition correlated to Curie temperature [2]. BST has been used successfully in high voltage capacitors, tunable filters, detectors, piezoelectrics, sensors, pressure transducers, actuators, and optoelectronic devices [3–7].

Controlling the amount of n-type (donor) and p-type (acceptor) dopants of pure barium titanate (BT) materials can modify semiconductor behavior. In order to improve the electrical properties of pure barium titanate, different types of donor or acceptor dopants have been employed. Small amounts of donor dopant at the A ( $\text{Ba}^{2+}$ ) site ( $\text{La}^{3+}$ ,  $\text{Ce}^{3+}$ ,  $\text{Dy}^{3+}$ ,  $\text{Nd}^{3+}$ ,  $\text{Gd}^{3+}$ ,  $\text{Sm}^{3+}$ ,  $\text{Y}^{3+}$ ) or acceptor dopant at the B ( $\text{Ti}^{4+}$ ) site ( $\text{Zr}^{4+}$ ,  $\text{Sn}^{4+}$ ,  $\text{Nb}^{5+}$ ,  $\text{Sb}^{5+}$ ,  $\text{Ta}^{5+}$ ) in a barium titanate structure have been investigated for a better understanding of semiconducting behavior (minimum resistivity occurrence is at room temperature for dopant at  $\text{Ba}^{2+}$  or  $\text{Ti}^{4+}$  positions) [8]. The electronic properties of  $\text{Ba}_x\text{Sr}_{1-x}\text{TiO}_3$  can be modified when  $\text{Sr}^{2+}$  partially substitutes  $\text{Ba}^{2+}$  in pure  $\text{BaTiO}_3$ . Besides the doping process, the electrical properties of BT are affected by microstructure, grain size, and compositional design [9].

Barium strontium titanate ( $\text{Ba}_x\text{Sr}_{1-x}\text{TiO}_3$ ) is a versatile material that is studied intensively nowadays for a variety of sensor applications, such as piezoelectric, pyroelectric, humidity, and gas sensing [10–13]. BST nanostructures have been synthesized by various methods or processes, such as sol-gel [14], co-precipitation [15], solvothermal [16], reverse microemulsion [17], pulsed laser deposition [18], ball milling [19], and hydrothermal techniques [20,21].

Hydrothermal technology has the advantage of producing powders with a high degree of crystallinity, fine particle size, and narrow particle size distribution. By varying the synthesis parameters, such as reaction temperature, time, and pH values, one can control the synthesis process. The available precursors for  $\text{BaSrTiO}_3$  preparations in hydrothermal conditions are inexpensive and easy to handle. For this reason, the hydrothermal synthesis of  $\text{BaSrTiO}_3$  is the best option taking into account the economic and technological aspects [22].

In our study, the doping mechanism is achieved by partial substitution of  $\text{Ba}^{2+}$  ions (A site) by  $\text{Sr}^{2+}$  and  $\text{Ti}^{4+}$  ions (B site) by  $\text{Co}^{3+}$  in the  $\text{ABO}_3$  structure using hydrothermal processes [10]. Thus, an excess of free charge carriers is created. This paper aims to investigate the microstructural, thermal, and gas sensing properties of nanostructured ( $\text{Ba}_{0.75}\text{Sr}_{0.25}$ ) ( $\text{Ti}_{0.95}\text{Co}_{0.05}$ )  $\text{O}_3$  perovskite powder (Co-doped  $\text{BaSrTiO}_3$ ) synthesized by the hydrothermal method. Electrical and thermodynamic characterization (by Differential Scanning Calorimetry (DSC) for mass loss and transient plane source for thermal conductivity) allows the evaluation of thermodynamic stability and the correlation of structural features with electrical conductivity under gas conditions. Two possible mechanisms of carbon dioxide ( $\text{CO}_2$ ) detection are then proposed under real operating conditions (i.e., in the presence of 50% relative humidity (RH)).

Carbon dioxide ( $\text{CO}_2$ ) is a colorless, inert gas. Along with other natural gases, it is a greenhouse gas, which is likely to occur either naturally (via organic matter decomposition) or from human activities (such as fossil fuel burning for power generation, oil refining, natural gas production, and/or transportation). When the  $\text{CO}_2$  concentration is higher in the surrounding atmosphere, a direct impact is likely to occur through global climate changes. The maximum limit of  $\text{CO}_2$  required by safety regulations within a gaseous mixture of other potential interfering agents found in mines must be between 5 to 20%. Beyond this limit,  $\text{CO}_2$  becomes hazardous for working personnel. Among the already mentioned issues, one should keep in mind that the direct impact of  $\text{CO}_2$  release in the atmosphere is leading to global climate changes, such as the greenhouse effect and global warming [23]. Therefore, one of the major scientific concerns in the gas-sensing field is linked to the possibility that the qualitative and quantitative detection of  $\text{CO}_2$  is of substantial interest in various fields by using gas sensors capable of detecting low traces under different working conditions [24]. State of the art  $\text{CO}_2$  detection comes at a high price, or with complicated operation mode sensors [25–27] or low selective

chemo-resistive sensors operating at high temperatures [28,29]. In the present paper, we report a simple, sensitive, and room temperature operating chemo-resistive CO<sub>2</sub> sensor, based on Co-doped BaSrTiO<sub>3</sub> obtained by a simple and low-cost technology.

## 2. Materials and Methods

### 2.1. Co-Doped BaSrTiO<sub>3</sub> Hydrothermal Synthesis

Nanostructured perovskite material (Ba<sub>0.75</sub>Sr<sub>0.25</sub>)(Ti<sub>0.95</sub>Co<sub>0.05</sub>)O<sub>3</sub> encoded as BSTCo5 was synthesized in a one-step process by hydrothermal method starting from water-soluble salts of Ti, Ba, Sr, and Co, respectively. TiCl<sub>4</sub> (Sigma-Aldrich, St. Louis, MI, USA, p.a. 98%), Sr(NO<sub>3</sub>)<sub>2</sub> (Merck, Kenilworth, NJ, USA, p.a. >99%), and Ba(OH)<sub>2</sub>·8H<sub>2</sub>O (Merck, e p.a. >98%) were used as precursors, and KOH was used as a mineralizer. The amounts of Ba(OH)<sub>2</sub>·8H<sub>2</sub>O, Sr(NO<sub>3</sub>)<sub>2</sub>, Co(NO<sub>3</sub>)<sub>2</sub>·6H<sub>2</sub>O (Sigma-Aldrich, p.a. >99%), and TiCl<sub>4</sub> were established in agreement with the theoretical molar formula (Ba<sub>0.75</sub>Sr<sub>0.25</sub>)(Ti<sub>0.95</sub>Co<sub>0.05</sub>)O<sub>3</sub>. The precipitation reaction pH was in the range of 9.5–13. The suspension thus obtained was subjected to hydrothermal processing (pressure 40 atm, temperature 200 °C, and time 2 h). The final suspension was introduced into a Teflon vessel of a sealed hydrothermal autoclave reactor (5 L, Berghof Products + Instruments GmbH, Berghof, Germany (Figure 1)) endowed with a cooling system. To control the reaction pressure, argon gas was purged inside the autoclave, according to working procedure described in [30].



**Figure 1.** The Berghof autoclave experimental device.

The Teflon vessel was filled to 80% of its capacity. To control the size and shape of the particles, after hydrothermal treatment, the autoclave was cooled at 2 °C/min until it reached 50 °C.

The wet precipitate was then filtered, washed with distilled water, and dried in an oven at 100 °C for 8 h, followed by hydrothermal synthesis. In order to study nanostructured powder behavior during thermal treatment, samples of the as-obtained BSTCo5 were subjected to heat treatment at either 800 °C and 1000 °C for two hours, and the samples were encoded as BSTCo5\_800 and BSTCo5\_1000, respectively. The optimum parameters for powder processing of RF-sputtering targets were selected after a close analysis of all the thermodynamic, morphological, and structural data.

### 2.2. Deposition Method of Sensing Layer

The Co-doped BaSrTiO<sub>3</sub> perovskite powder obtained as described above, was processed and pellets of 5.08 cm (2 inches) were obtained under 5 tons/cm<sup>2</sup> force. In order to be used as targets in the

RF sputtering process, the pellets were then sintered for one hour at 1000 °C. The RF sputtering system consisted of a TORUS 2HV magnetron source, KJLC 300 W Kurt J. Lesker power supply, VUP-5 vacuum installation, mounting and rotating supports, and a cathode cooling system. Thin films were deposited under 75 W sputtering power, 150 VDC, and 10 Pa argon vacuum conditions onto commercial Al<sub>2</sub>O<sub>3</sub> substrates (Metrohm DropSens, Oviedo, Spain) provided with Au interdigital electrodes for measuring the sensitive layer resistance and Pt heaters for holding the sensor at the desired operating temperature (Figure 2a). The thin films were deposited under a controlled speed over 3 h and further heat-treated for 20 min at 800 °C under vacuum conditions in order to improve film adherence and crystallinity (BI no. 131119/30.07.2019) [31].

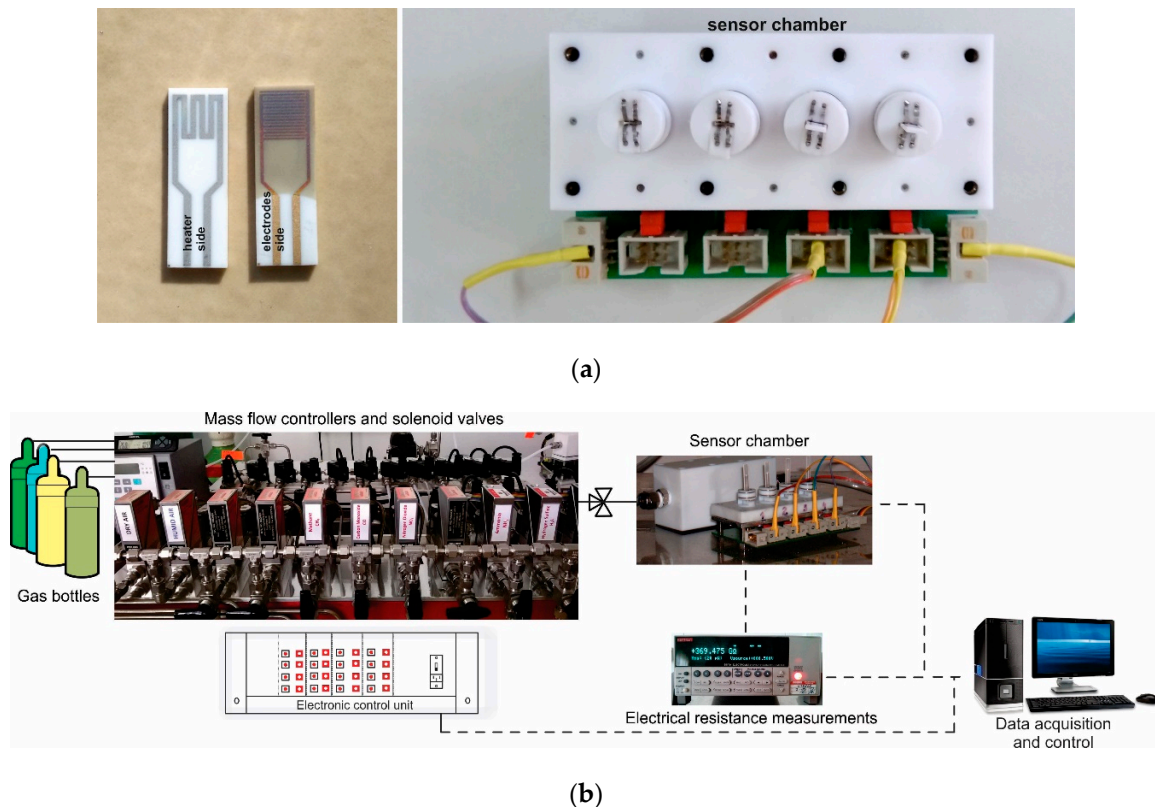


**Figure 2.** (a) Details about electrical connections of the sensor chamber and sensor layout; (b) Gas mixing system workbench with data acquisition.

### 2.3. Characterization

Powders were characterized from the chemical point of view by the Inductively Coupled Plasma Atomic Emission Spectroscopy (ICP-OES) technique, using ICP-OES 725 (AGILENT, Santa Clara, California, SUA) equipment, according to ASTM E 1479-16 standards.

The microstructure of the powders was examined using a Bruker D8 ADVANCE (Bruker AXS GmbH, Karlsruhe, Germany) X-ray Diffractometer with Bragg–Brentano geometry using Cu-K $\alpha$  characteristic radiation and equipped with a scintillation counter and a graphite monochromator. The data was collected at a step size of 6 s per step and a collection angle  $2\theta = 20^\circ\text{--}80^\circ$ , at room temperature. The data acquisition and the identification of the phases contained within the samples was performed using the software package DIFFRAC SUITE.EVA (5.1 Bruker AXS GmbH, Karlsruhe, Germany) and the ICDD PDF-4+ 2020 database, edited by the International Center for Diffraction Data (ICDD).

The UV Raman spectra were collected by means of a LabRAM HR800 (HORIBA FRANCE SAS, Palaiseau, France) spectrometer equipped with a CCD HeCd laser (325 nm) from Kimmon Koha (Tokio,

Japan) and a 2400 grating. A microscope objective with magnification of 40× NUV (NA 0.47) from Olympus (Tokyo, Japan) was used to focus the laser light on the samples.

Scanning Electron Microscopy was performed using a FEI Quanta 250 (FEI Company, Eindhoven, Netherlands) high resolution microscope incorporated with an Energy Dispersive X-Ray Spectrometer, produced by EDAX Ametek (Mahwah, NJ, USA), consisting of an Element Silicon Drift Detector and a Team 4.5 EDS Analysis System (EDAX Ametek, Mahwah, NJ, USA). The samples were prior coated with a thin gold layer in order to improve the conduction of the sample.

Size distribution of the material was measured by DLS instrument (Zetasizer Nano ZS90; Malvern Instruments, Malvern, UK) using a 4 mW He-Ne laser at a wavelength of 632.8 nm. Briefly, 0.05 g of the sample was mixed with deionized water, ethanol, and poly(acrylic acid sodium salt) solution from Sigma-Aldrich (St. Louis, MI, USA) in a predetermined proportion.

The thermal behavior of Co-doped BaSrTiO<sub>3</sub> samples under nonisothermal conditions was investigated by Differential Scanning Calorimetry (DSC) and thermogravimetry (TG) using SETSYS Evolution 17 (Setaram, Caluire-et-Cuire, France) equipment. The heat flow was calibrated and adjusted at different temperatures using certified materials at 3 heating rates. The samples were heated in alumina crucibles, in a temperature range from 25 to 1200 °C, under a constant flow of pure argon (16 mL/min), and a 10 K min<sup>-1</sup> heating rate.

Thermal conductivity was measured at room temperature by transient plane source using the hot disk method (TPS 2200, Hot Disk, Göteborg, Sweden) on pairs of cylindrical samples (11 mm diameter and 6 mm height) heat-treated at 800 °C. Briefly, a 2 mm diameter hot disk Kapton sensor (code 7577) sandwiched between the two cylindrical replicate samples was used to simultaneously generate heat and monitor the temperature changes. The method directly measured the thermal conductivity, using a calculation algorithm implemented by the manufacturer as the instrument data processing software.

Gas sensing properties of previously obtained sensors were placed into the sensor chamber (Figure 2a) and evaluated under real operating conditions (the presence of relative humidity and other potential interfering gases) simulated in the laboratory using a dynamic Gas Mixing System (GMS) [32]. The total flow through the system consisted of mixed user-defined gas types and could be adjusted up to 200 mL/min. The CO<sub>2</sub> gas concentrations could be adjusted from 400 to 3000 ppm, whereas other potential interfering gases at their specific detection limit ppm levels (CO, CH<sub>4</sub>, NO<sub>2</sub>, H<sub>2</sub>S, NH<sub>3</sub>, and SO<sub>2</sub>) were dosed in synthetic air (purity 5.0) with variable relative humidity (0–50% RH). Real-time data acquisition of the electrical resistance changes was acquired using a Keithley Electrometer 6517A (Cleveland, Ohio, USA) (see Figure 2b).

### 3. Results and Discussion

Chemical, morphological, structural, thermal, and conductivity analyses were performed to better understand the behavior of the nanostructured powder during processing and deposition by RF sputtering. The results are presented below.

#### 3.1. Chemical Composition of Co-Doped BaSrTiO<sub>3</sub> Powder

Chemical composition was determined for Co-doped BaSrTiO<sub>3</sub> as obtained by hydrothermal procedure. Ba, Sr, Ti, Co were determined by ICP-OES and CO<sub>3</sub><sup>2-</sup> was determined by gravimetric analysis. CO<sub>3</sub><sup>2-</sup> analysis (0.8 ± 1%) indicated a 96% powder purity.

Spectroscopy was carried out according to ASTM E1479-16. The results of elemental analysis are presented in Table 1.

**Table 1.** The results of elemental analysis determined by ICP-OES.

Chemical Analysis wt.%			
Ba	Sr	Ti	Co
41.2 ± 0.5	10.2 ± 0.7	21.1 ± 0.4	1.35 ± 0.3

### 3.2. X-ray Diffraction of Co-Doped BaSrTiO<sub>3</sub> Powder

Figure 3 illustrates patterns of BSTCo5, BSTCo5\_800, and BSTCo5\_1000.

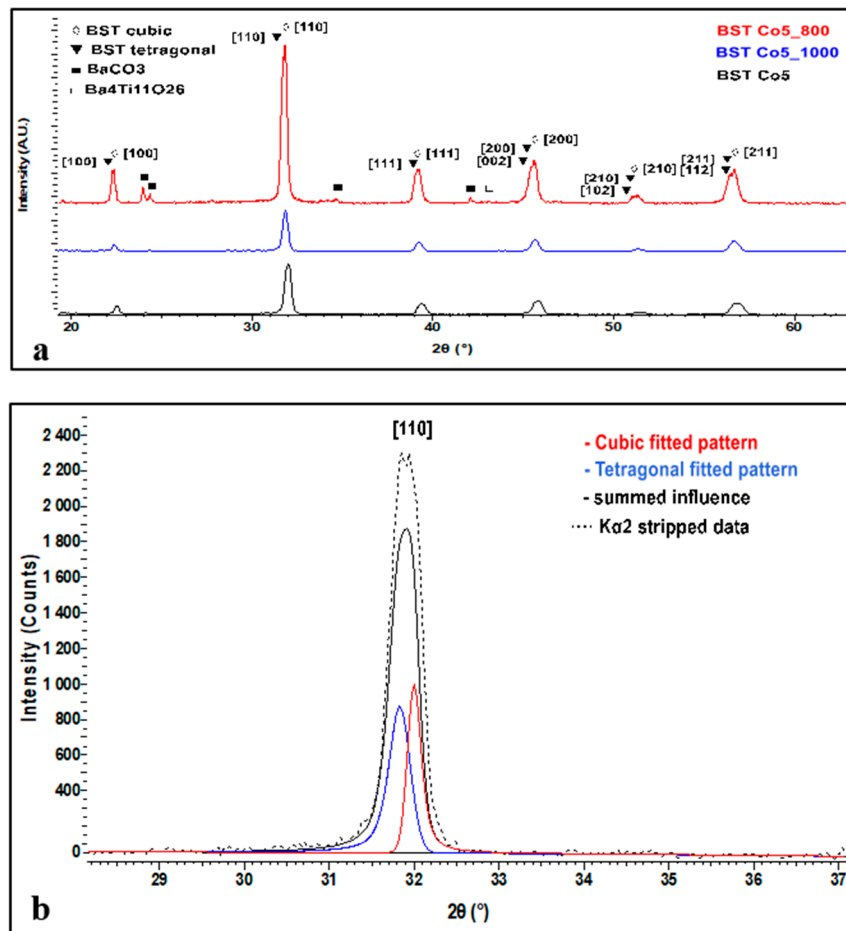


**Figure 3.** XRD analysis of BSTCo5, BSTCo5\_800, and BSTCo5\_1000 (a), details of the cubic-tetragonal structure (b).

The main reflections at  $2\theta$  around  $22^\circ$ ,  $31^\circ$ ,  $38^\circ$ , and  $45^\circ$  can be indexed with both tetragonal (P4mm PDF 70-9164) and cubic (Pm-3m PDF 70-9165) polymorphs of the perovskite material. Since the intensity of the main diffraction peak of the BaCO<sub>3</sub> phase is quite weak, this indicates traces of this phase in the sample.

The XRD spectrum in Figure 3a presents all diffraction peaks related to the BST phase. In general, the sample related contribution to the diffraction peak profiles is often described as a combination of Gauss and Lorentz (Cauchy) functions. When viewing the profile of the peaks, it is clear that they are affected by the influence of two or more phases. Thus, in Figure 3b, we present the fitted patterns of both cubic and tetragonal peaks related to the [110] crystallized plane, which precisely explains the peak profile and shape. This clearly indicates the presence of both structures.

For Co-doped BaSrTiO<sub>3</sub>, on the [110] crystallization direction, the crystallite size was calculated by taking into consideration a split pseudo-Voigt type of function and using Scherrer equation with consideration to the FWHM. The calculated crystallite size was around 43.5 nm for the cubic structure and around 27.8 nm for the tetragonal structure.

One can observe in the sample heat-treated at 1000 °C (encode BSTCo5\_1000) that a small amount of secondary phase Ba<sub>4</sub>Ti<sub>11</sub>O<sub>26</sub> (PDF 83-1459) appears (low-intensity diffraction lines at  $2\theta$  angles 27 and  $30^\circ$ ).

In literature, this phase appears in  $\text{Fe}_2\text{O}_3$  doped  $\text{BaTiO}_3$  powder [33]. This phase was also identified in a  $(\text{Ba}_{0.2}\text{Sr}_{0.2}\text{Ca}_{0.2}\text{Mg}_{0.2}\text{Pb}_{0.2})\text{TiO}_3$  perovskite compound when it was heat-treated at  $1400\text{ }^\circ\text{C}$  [34] in an Sb-doped barium strontium titanate powder (with  $\text{TiO}_2$  and  $\text{SiO}_2$  excess), which was heat-treated at  $1000\text{ }^\circ\text{C}$  [35]. If we take into account the aforementioned studies, it seems to be a high-temperature related phase.

XRD investigation completes the result given by the elemental chemical composition analysis. The target compound was not subjected to XRD analysis as previous experience indicated that the presence of  $\text{BaCO}_3$  in BST heat-treated samples diminishes almost entirely [13].

The XRD pattern of the BST sample obtained by the hydrothermal method is presented in Figure 3.

### 3.3. UV Raman Spectroscopy for Co-Doped $\text{BaSrTiO}_3$ Powder

UV Raman spectroscopy (Figure 4) is a very sensitive technique for the surface investigation of materials, especially nanoscale ferroelectrics and their thin films [34].

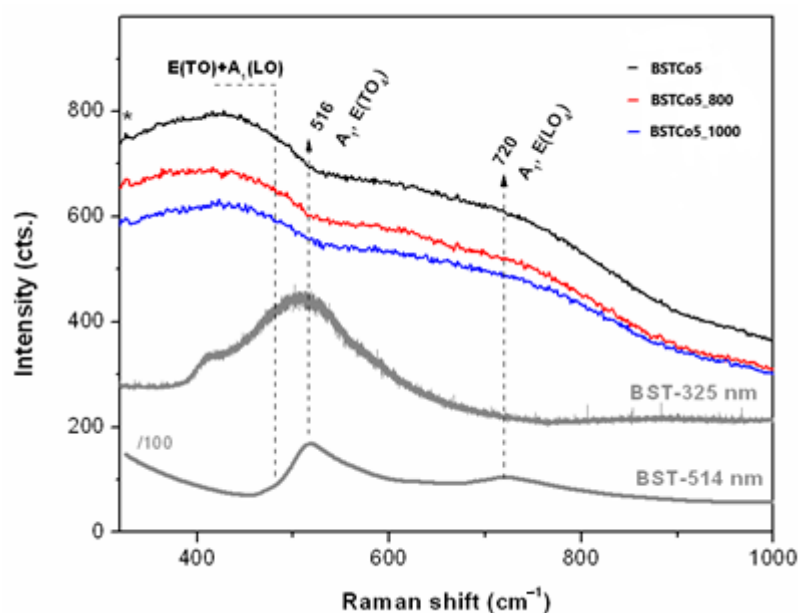


**Figure 4.** UV Raman spectra of the BST5Co samples compared with BST (\*325 nm laser lines).

UV Raman spectra of the Co-doped  $\text{BaSrTiO}_3$  were compared with those of pure BST in order to investigate the Co dopant influence on the BST structure, as illustrated in Figure 4. Both pure BST and BSTCo5 were synthesized under the same conditions.

Pure BST samples were excited with 325 and 514 nm laser lines. In both cases, the presence of cubic and tetragonal phases was observed. In the case of Co-doped BST samples, only the 325 nm laser source was used. The vibration corresponding to the tetragonal structure was not identified. In this case, it could be considered that the cubic phase was predominant.

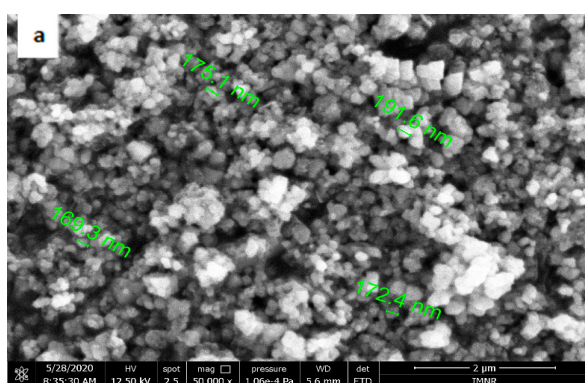
Thus, given the forbidden Raman activity of the cubic  $\text{ABO}_3$  [36,37], the presence of a limited number of bands in Figure 4 indicated second-order Raman modes of the disordered cubic  $\text{BaTiO}_3$  (BT) in the as-obtained BST5Co5 sample. Wider bands were recorded for the BST5Co\_800 sample. Typically, Raman spectrum of BT is divided into two ranges, below  $250\text{ cm}^{-1}$  (cationic network and the lattice modes) and within the  $200\text{--}800\text{ cm}^{-1}$  range, which is due to the bending and stretching modes of the oxygens in the covalent linked  $\text{BO}_6$  octahedra in  $\text{ABO}_3$  [38]. However, the edge filter prevented recording of the UV Raman spectra at low wavenumbers. Moreover, BT and  $\text{SrTiO}_3$  (ST) had several active modes close to each other [39]. The  $\text{TO}_4$  modes presented in the BST spectra in Figure 4 vanished for BST5Co samples where cubic structure prevailed. This was similar to the second-order spectral

features reported for the paraelectric BT layers in the BaTiO<sub>3</sub>/SrTiO<sub>3</sub> superlattices at temperatures exceeding T<sub>c</sub> (>250 °C) [40]. Co-doping of the BST triggered the formation of the cubic phase.

The results obtained from the Raman analysis are in agreement with the results obtained by the XRD analysis.

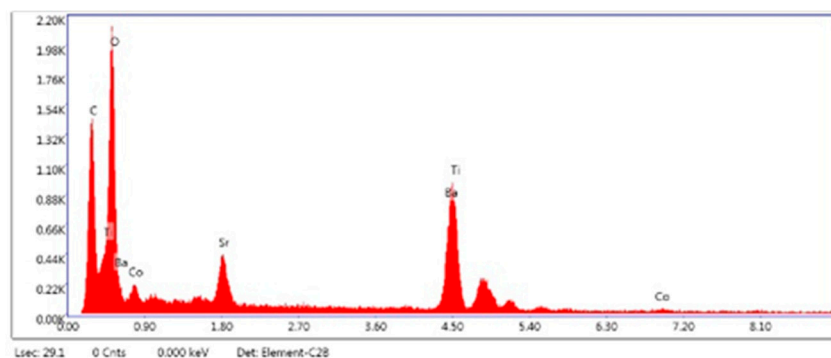
### 3.4. Scanning Electron Microscopy for Co-Doped BaSrTiO<sub>3</sub> Powder

Figure 5 shows the results of morphological and structural analysis by Scanning Electron Microscopy. It can be seen that the BSTCo5 sample obtained in hydrothermal conditions contains aggregates of faceted particles with dimensions in the range of 170–190 nm. The morphology of the sample BSTCo5 is influenced by the heat treatment temperature (Figure 5b,c). In the sample that is heat-treated at 800 °C, particles have dimensions in the range 230–400 nm, and no important particle growth can be observed for the sample heat-treated at 1000 °C (290–560 nm). Thermal treatment temperature does not influence significantly the size of the particle.

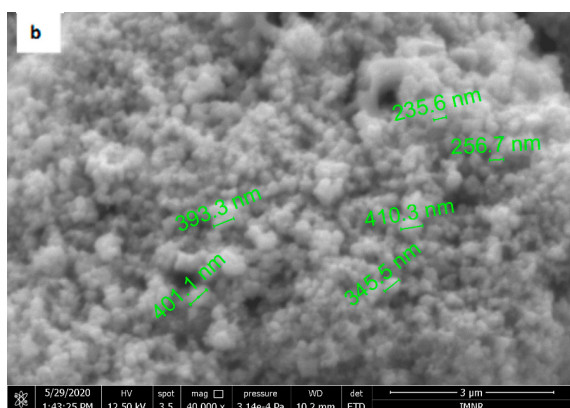


Element	Weight %	Atomic %	Net Int.
C K	19.53	37.94	376.29
O K	33.37	48.65	564.17
Sr L	4.34	1.16	85.72
Ba L	26.79	4.55	162.00
Ti K	15.16	7.38	272.35
Co K	0.80	0.32	5.67

(a)



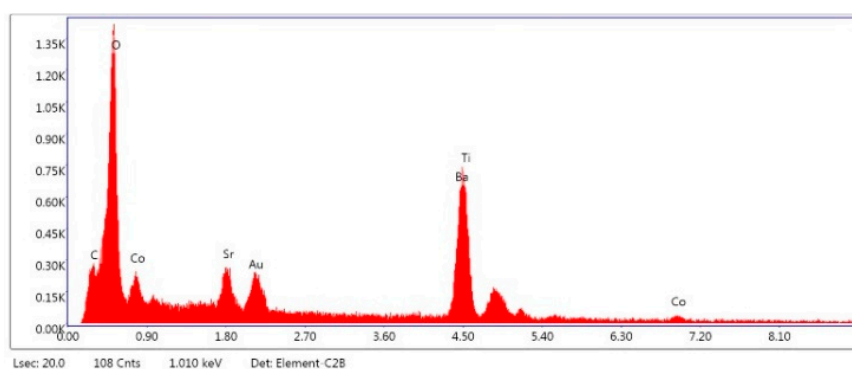
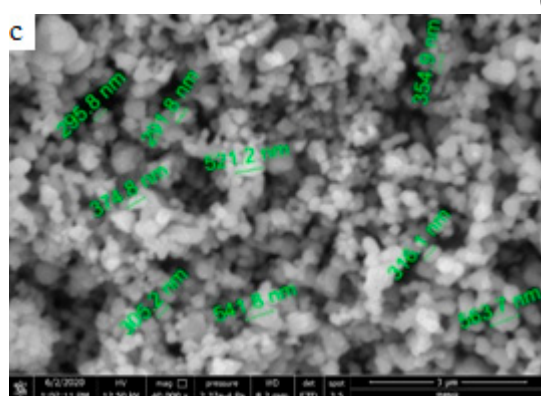
(a2)



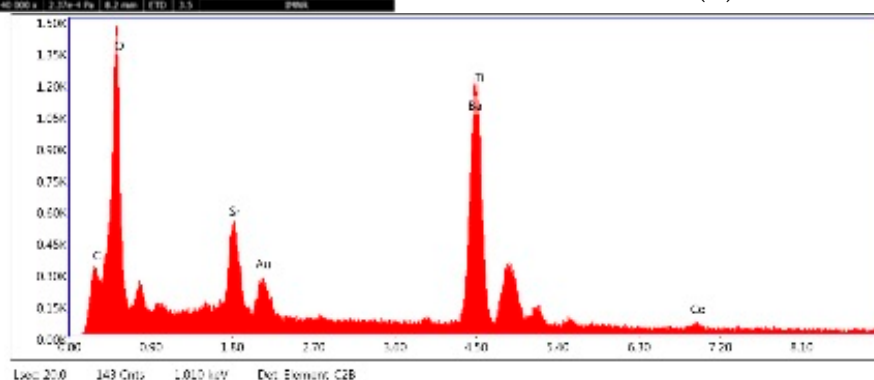
Element	Weight %	Atomic %	Net Int.
C K	3	9.35	92.75
O K	22.71	53.03	588.12
Sr L	4.61	1.97	92.98
Au M	5.95	1.13	83.28
Ba L	28.87	7.85	128.45
Ti K	31.33	24.44	409.54
Co K	3.52	2.23	14.28

(b<sub>1</sub>)

Figure 5. Cont.

(b<sub>2</sub>)

Element	Weight %	Atomic %	Net Int.
C K	5.69	15.90	144.08
O K	26.30	55.16	640.18
Sr L	7.65	2.93	234.28
Au M	4.02	0.69	91.35
Ba L	30.57	7.47	298.49
Ti K	24.29	17.01	687.42
Co K	1.48	0.84	16.83

(c<sub>1</sub>)(c<sub>2</sub>)

**Figure 5.** Scanning Electron Microscopy/EDAX analysis for BSTCo<sub>5</sub>, BSTCo<sub>5\_800</sub>, and BSTCo<sub>5\_1000</sub>: (a–c) Scanning Electron Microscopy for BSTCo<sub>5</sub>, BSTCo<sub>5\_800</sub>, and BSTCo<sub>5\_1000</sub>; (a<sub>1</sub>–c<sub>1</sub>) tables of EDAX elemental content for BSTCo<sub>5</sub>, BSTCo<sub>5\_800</sub>, and BSTCo<sub>5\_1000</sub>; (a<sub>2</sub>–c<sub>2</sub>) EDAX mapping for BSTCo<sub>5</sub>, BSTCo<sub>5\_800</sub>, and BSTCo<sub>5\_1000</sub>.

The presence of two primary BST phases, cubic and tetragonal, identified by XRD analysis, likely hinders the particle growth [41]. The presence of Ba, Sr, Ti, and Co elements in each sample is shown in Figure 5. The EDAX analysis is in agreement with the XRD and chemical elemental analyses.

### 3.5. Dynamic Light Scattering Analysis for BSTCo<sub>5</sub> Powder

The DLS analysis indicates the presence of nanosized particles by completing the information obtained by SEM analysis, providing essential data in the processing and determination of sensitive properties. Stable suspension based on BSTCo<sub>5</sub> was prepared for the DLS measurements.

Hydrodynamic diameter of spherical particles can be defined using the Stokes–Einstein equation:

$$d_H = kT/3\eta\pi D \quad (1)$$

where  $d_H$  = hydrodynamic diameter,  $k$  = Boltzmann's constant ( $1.38 \times 10^{-23} \text{ NmK}^{-1}$ ),  $T$  = absolute temperature (K),  $\eta$  = solvent viscosity ( $\text{N}\cdot\text{s}\cdot\text{m}^{-2}$ ), and  $D$  = diffusion coefficient ( $\text{m}^2\cdot\text{s}^{-1}$ ).

Figure 6 shows the particle size distribution by DLS analysis for the Co-doped BST sample. The particle size is in the range between 10 and 78 nm, and the calculated average hydrodynamic diameter of the nanoparticles is 24 nm (Figure 6). It is well known that nanoparticles based on  $\text{BaTiO}_3$  are prone to aggregation caused by interparticle interactions due to van der Waals forces [40].

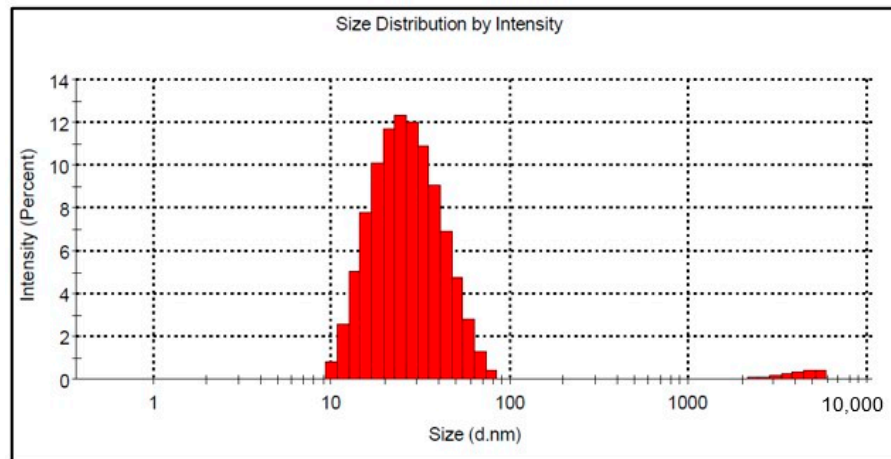


Figure 6. Mean size of BSTCo5 particles in suspension.

By corroborating the XRD analysis for crystallite size with DLS analysis for BSTCo5, one can say that the sample is nanostructured, as presented by Simões et al. [41] for BST powder.

### 3.6. Differential Scanning Calorimetry and Thermogravimetry Analysis for BSTCo5 Powder

Hydrothermal obtained powders were used for RF sputtering target processing (pressing and sintering). The main reason these powders were subjected to thermal analysis was to determine the powder stability and phase transformations.

The TG and DSC plots of the Co-doped BST powders heated from ambient temperature to 1200 °C are shown in Figure 7. Several mass losses are revealed in the TG curve, presented in Table 2. A first step is the release of adsorbed water in the range of 27–280 °C, the value of weight change being 0.6%. A second step, occurring from 280–450 °C, corresponds to a total weight loss of 0.5% and results from the release of chemisorbed water or hydroxyl groups. Between 450 and 730 °C, there is no mass loss, and between 730 and 870 °C, there is a mass loss of about 0.9% that is likely correlated with the polymorphic transformation of  $\text{BaCO}_3$  [42], and is also identified by XRD analysis. No weight loss is registered in the range of 870–1200 °C.

Table 2. Heat flow and mass loss for BSTCo5.

Temperature (°C)	$\Delta H$ (J/mol)	Mass Loss (mg)	Mass Loss (%)	Observation
27–280	-	0.069	0.6	Release of Adsorbed Water
280–450	-	0.064	0.5	Chemisorbed Water or Hydroxyl Groups
450–730	-	-	-	No Mass Loss
836	8038	0.121	0.1	Polymorphic Transformation of $\text{BaCO}_3$

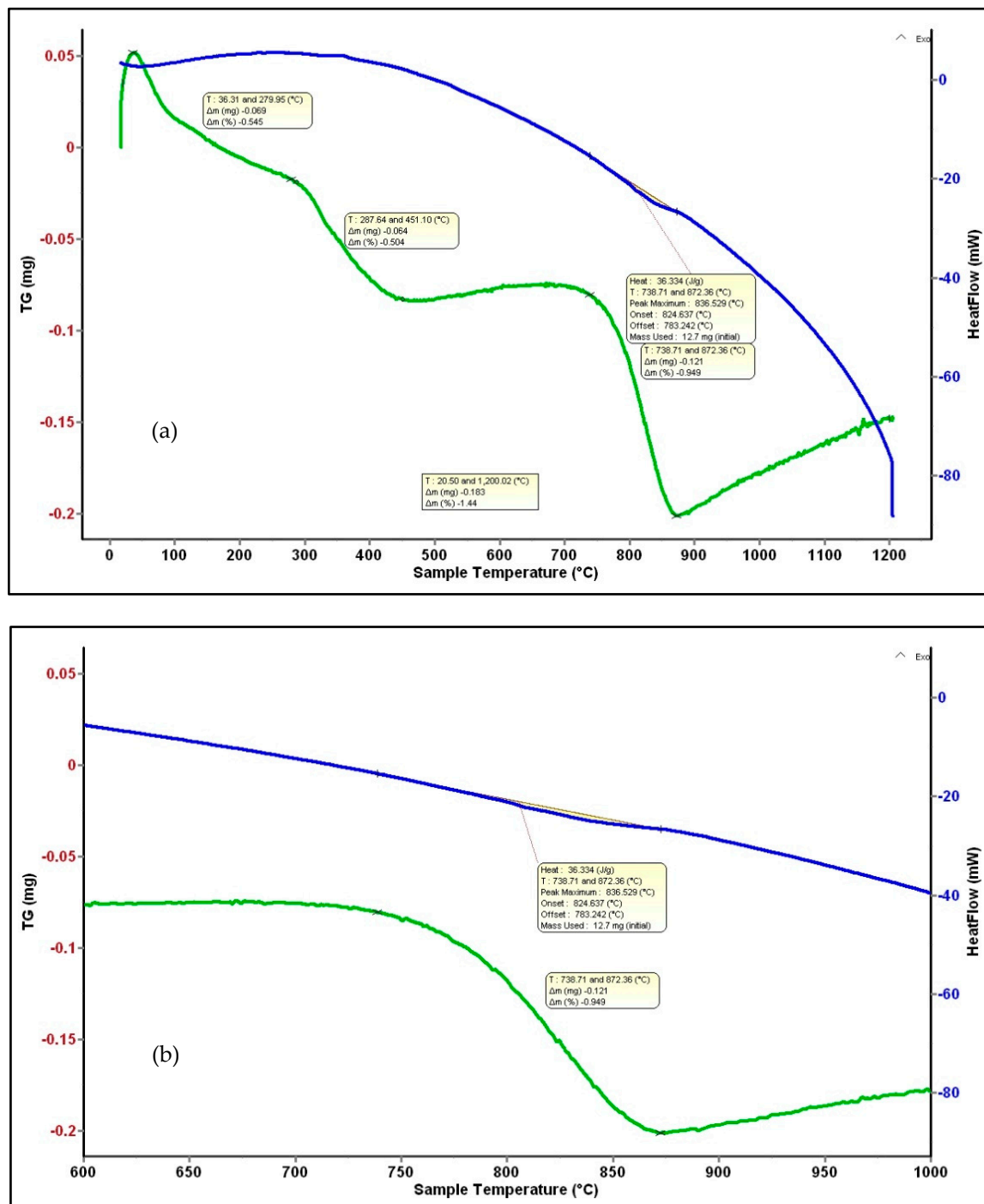


**Figure 7.** DSC-TG analysis of BSTCo5 powder (a) and a detail for the mass loss corresponding to the 836 °C peak (b).

### 3.7. Thermal Conductivity Analysis for BSTCo5 Powder

The specific heat of the Co-doped BST material is used for estimating the thermal inertia of the sensitive layer of the sensor, with the aim of a quick sensor cleaning protocol. Thermal conduction in the sensing material also plays an important role in dissipating heat.

BSTCo5 samples treated at 800 °C were subjected to thermal conductivity, thermal diffusivity, and volumetric specific heat analysis (Table 3). Based on the volumetric specific heat, the specific heat

of the BSTCo5 sample was calculated. Ten successive measurements were performed in order to obtain the values in Table 3.

**Table 3.** Thermal conductivity, thermal diffusivity, volumetric specific heat, and specific heat determined at room temperature.

Material	k (W/mK)	$\alpha$ (mm <sup>2</sup> /s)	Volumetric Cp (10 <sup>6</sup> J/m <sup>3</sup> K)	Cp (J/gK)	Ref.
BSTCo5	0.40 ± 0.01	0.26 ± 0.02	1.513 ± 0.09	0.576	Present work [42]
BT Provider A	2.61 ± 0.02	1.03 ± 0.01	2.532 calculated	0.434 ± 0.004	
BT Provider B	2.85 ± 0.04	1.18 ± 0.02	2.411 calculated	0.406 ± 0.008	

The thermal conductivity (room temperature) of the BSTCo5 sample is 0.4 W/(mK). Compared with a similar chemical compound, BaTiO<sub>3</sub>, this is smaller than the values of 2.61 to 2.85 W/(mK) reported by others some decades ago [43], but it is consistent with recent data presented by Shirane [44]. The value of 0.576 (J/gK) for specific heat is in good agreement with the literature reports of Popescu et al. [45] and Shirane et al. [44], and it is consistent with literature data of pure BaTiO<sub>3</sub> [43–46]. Accordingly, the 0.26 (mm<sup>2</sup>/s) value for thermal diffusivity is lower than 1.03 to 1.18 (mm<sup>2</sup>/s), reported by He [42] for BaTiO<sub>3</sub> samples. BT sample A represents BaTiO<sub>3</sub> (Supplier A), and BT sample B represents BaTiO<sub>3</sub> (Supplier B) [43].

The variation of the data can be attributed to: (a) dopants used for BaTiO<sub>3</sub> based material, (b) different manufacturing procedures leading to lower densities of the material and, to some degree, (c) techniques used for thermal conductivity measurement. To be more specific, a drop in thermal conductivity for Co-doped BST compared with BT can be explained by the influences of the dopant, which induce defects in the crystal structure.

### 3.8. CO<sub>2</sub> Sensing Properties

It is generally accepted knowledge that, for chemo-resistive sensors, the chemical interactions of gases are modulated by the temperature of the sensitive layers and determine the variation of their electrical resistance. Thus, the preliminary selection between BSTCo5\_800 and BSTCo5\_1000 sensors was assessed for a fixed CO<sub>2</sub> concentration of 3000 ppm in the temperature range of room temperature (RT) between 23 and 400 °C. CO<sub>2</sub> was dosed into synthetic airflow with 50% RH, an atmosphere similar to in-field background (real operating conditions). Accordingly, the sensor signal, defined as the relative measure of the sensitive layer resistance under CO<sub>2</sub> exposure ( $R_{\text{gas}}$ ) with respect to the reference atmosphere ( $R_{\text{air}}$ ), is represented in Figure 8a. As can be seen, the highest signal is obtained for the BSTCo5\_800 layer at room temperature (RT = 23 °C). A possible explanation is related to the specific structure and morphology of the samples inducing specific surface defects [46]. Despite the magnitude of the signal greater than 30 and the good response time, the electrical resistance of the BSTCo5\_800 layer does not return to its initial value after exposure to CO<sub>2</sub>, most likely due to the formation of irreversible carbonic acid at the surface (Figure 8b). A short temperature boost of 3 min (‘) at 300 °C ensures the cleaning of the surface and the return of the resistance, as seen in the inset from Figure 8b.

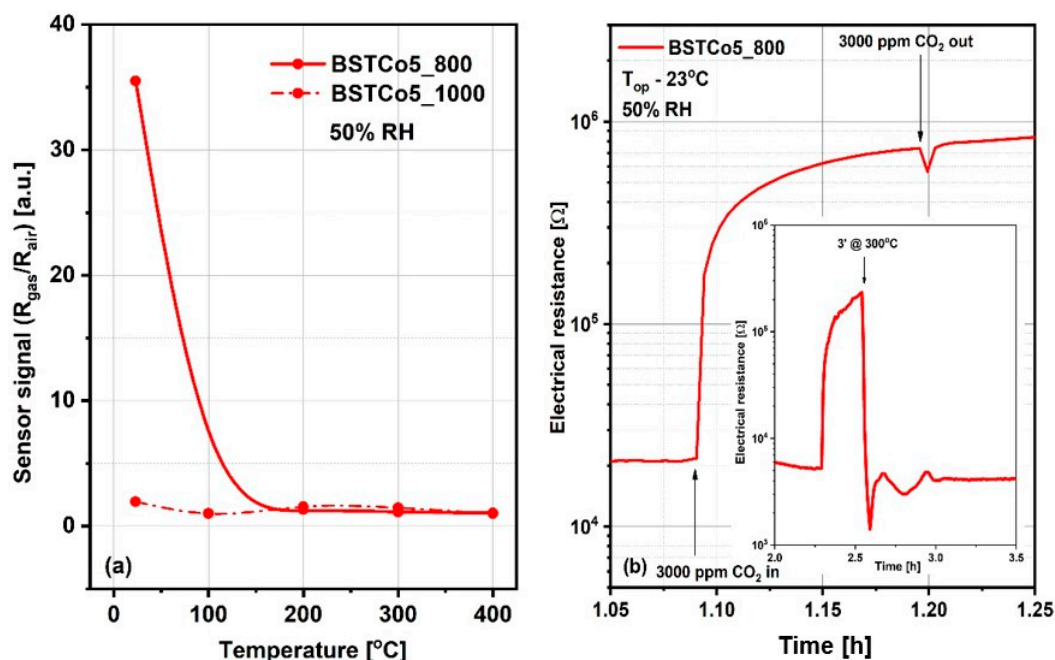
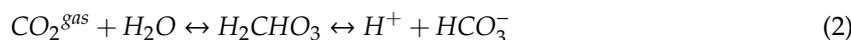


**Figure 8.** (a) Sensor signal for 3000 ppm CO<sub>2</sub> for temperature range 23–400 °C; (b) Surface contamination from exposure to CO<sub>2</sub> and the solution of 3 minutes at 300 °C temperature boost applied for its rapid cleaning (b-inset).

Knowing that CO<sub>2</sub> solubility in water at room temperature is around 1.25 g/kg H<sub>2</sub>O, the following relation may take place:



Alternatively, (see Figure 9) CO<sub>2</sub> reacts with hydrogen from the dissociated water. We note that the electric field specific to the electrical measurements is 15 kV/m.

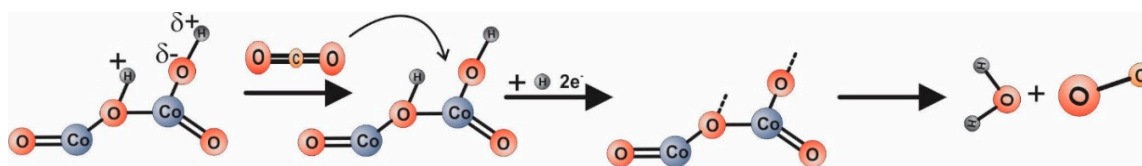


**Figure 9.** Possible conduction mechanism involved in CO<sub>2</sub> detection

For the case of Equation (2), the changes in electrical resistance are induced by water-mediated dipole interactions resulting from physisorbed water vapors from the atmosphere [44]. Such behavior is in good correlation with the water condensation phenomena triggered by the porous structure as revealed from the TG and DSC plots.

Knowing that nanoparticles based on BaTiO<sub>3</sub> are prone to aggregation, which is caused by inter-particle interactions due to van der Waals forces, capillary condensation of the water vapors occurs at the liquid-vapor equilibrium with respect to the Kelvin equation:

$$r = \frac{-2\gamma V_L \cos\theta}{RT \ln(p/p_0)} \quad (4)$$

where  $\theta$  is the contact angle between the liquid and the wall of the capillary pore,  $V_L$  represents the molecular volume of liquid,  $\gamma$  represents the water’s surface tension,  $R$  represents a gas specific constant,  $T$  represents the absolute temperature express in K, and  $r$  is the Kelvin radius of the capillary pores.

The case in Equation (3) explains the increase of resistance by electrons involved in  $CO_2$  decomposition in the presence of dissociated water (due to the high intensity of the electric field) [47].

Accordingly, the influence of the relative humidity level on the reference atmosphere ( $R_{air}$ ) as well as on the sensitive layer resistance under  $CO_2$  exposure ( $R_{gas}$ ) have been highlighted through electrical investigations, and prove that the value of 50% RH (known as medium level value for in-field atmosphere) constitutes the threshold of the  $CO_2$  detection regime (Figure 10). As can be seen in Figure 10a, the  $CO_2$  interaction is favored by the relative humidity, the threshold being 50% RH. The stability of the electrical resistance up to this threshold suggests the validity of the dipole interaction without the change of electric charge, described by Equation (2). Above this threshold, there is an increase in resistance following the exposure to progressive concentrations of  $CO_2$ , which demonstrates a decrease in the number of charge carriers, suggesting the validity of Equation (3). We have to mention that after each  $CO_2$  concentration, a short temperature boost of 3’ at 300 °C was applied for the cleaning of the surface and the return of the resistance, as explained for the Figure 8b. For the simplicity of Figure 10a, the moment of  $CO_2$  admission and the moment of the temperature boost is shown with arrows only for one of the four  $CO_2$  concentrations (400, 1000, 2000, and 3000 ppm). The response and recovery transients have also been calculated (see Table 4).

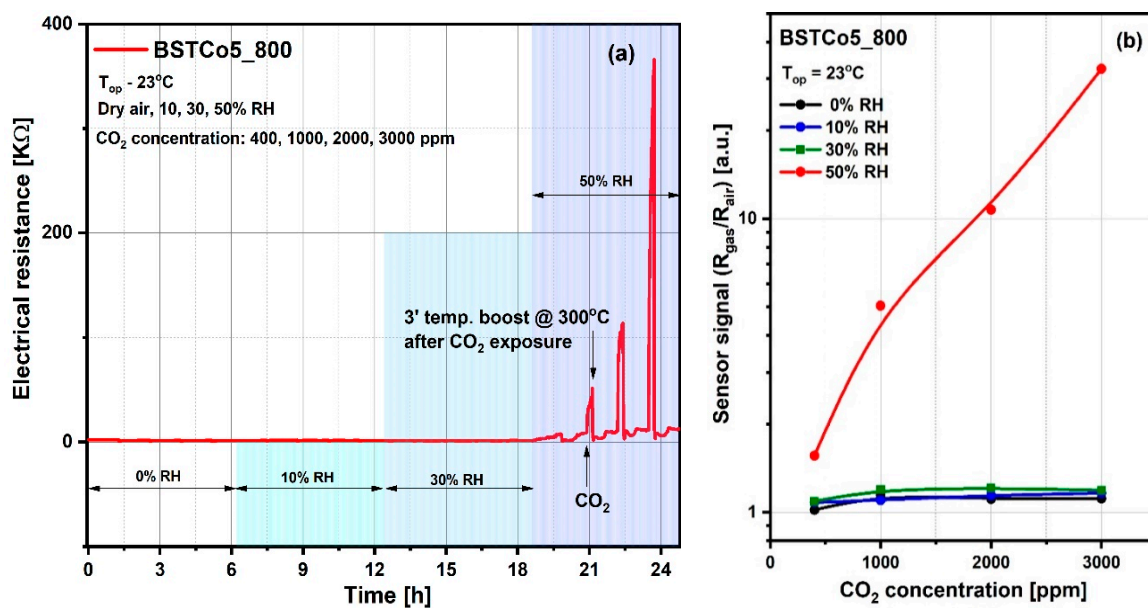


**Figure 10.** (a) Variations in electrical resistance for BSTCo5\_800 due to exposure to  $CO_2$  in atmospheres with variable relative humidity (0%, 10%, 30%, and 50% RH); (b) The sensor signal for 400–3000 ppm of  $CO_2$  under different relative humidity background conditions.

**Table 4.** Calculated response and recovery times related to the changes in the electrical resistance upon different  $CO_2$  concentration exposure as presented in Figure 10a.

50% RH	400 ppm $CO_2$		1000 ppm $CO_2$		2000 ppm $CO_2$		3000 ppm $CO_2$	
Transients	$\tau_{response}$	$\tau_{recovery}$	$\tau_{response}$	$\tau_{recovery}$	$\tau_{response}$	$\tau_{recovery}$	$\tau_{response}$	$\tau_{recovery}$
Minutes	9	8	13	7	6	7	12	8

The response time refers to the time needed to reach a stable sensor response after a stepwise increase in the test gas concentration. Hence, the response time is defined as the time  $\tau_{response}$  takes for 90% of the sensor’s electrical resistance to be accomplished.

The recovery time refers to the time the sensor needs for the sensor response to return to the base electrical resistance after removing the test gas. The recovery time is defined in a similar manner as the response time, namely  $\tau_{\text{recovery}}$  takes 90% of the sensor's electrical resistance to return to its base resistance.

The sensor signal (Figure 10b) is defined as the ratio between the electrical resistance under CO<sub>2</sub> exposure ( $R_{\text{gas}}$ ) and the electrical resistance under synthetic air with 50% RH ( $R_{\text{air}}$ ).

The sensor signal is represented for the range of CO<sub>2</sub> concentrations between 400 and 3000 ppm. The lower concentration of 400 ppm corresponds to the current safe level of CO<sub>2</sub> for outdoor ambient air. Typical safe concentrations for indoor spaces are 400–1000 ppm CO<sub>2</sub>, with upper levels between 1000 and 5000 ppm CO<sub>2</sub> causing headaches, sleepiness, loss of attention, increased heart rate, and slight nausea. Accordingly, to prevent the health risks associated with CO<sub>2</sub>, the imposed exposure limit is 5000 ppm [48].

The last step in evaluating the sensitive properties of BSTCo5\_800 was the selectivity analysis that highlighted the signal to CO<sub>2</sub> compared with the signals to other gases potentially present in the ambient atmosphere. For each of the gases, the test was performed at the specific detection threshold stipulated by European regulations (Figure 11).

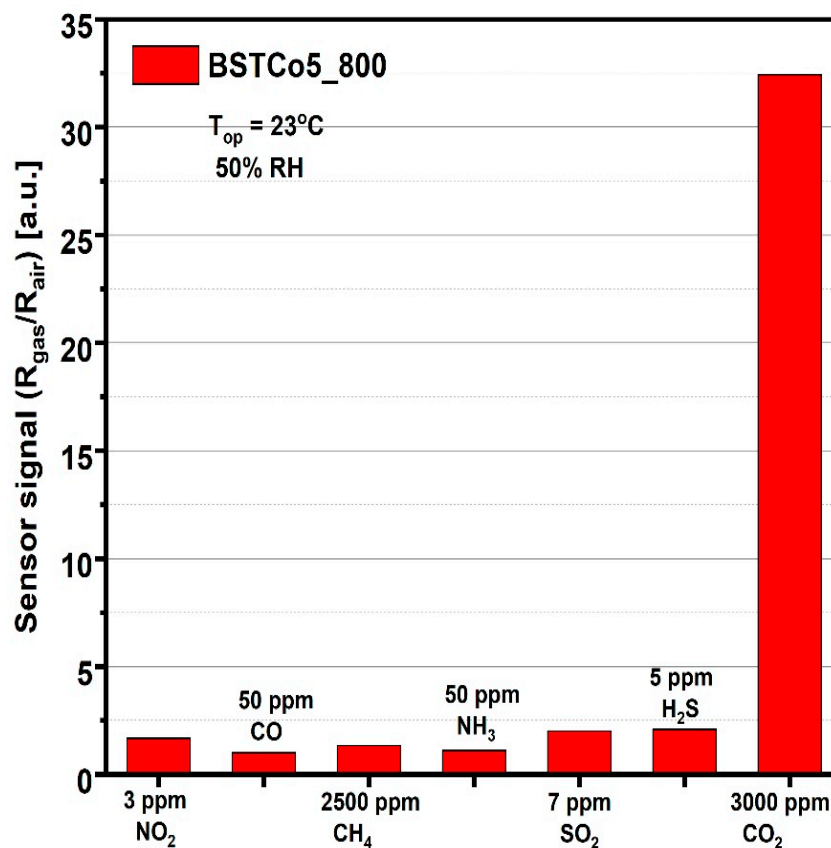


Figure 11. Sensor signal for 3000 ppm CO<sub>2</sub> and for other potential interfering gases.

Considering the simple and low-cost technology, the good signal under infield humidity conditions (Figure 10a), the high selectivity relative to other potential interfering gases (Figure 11), and the low power consumption corresponding to RT operation, we can say that BSTCo5\_800 has the potential for future portable detector development.

For other potential interfering gases, the concentrations were chosen according to the EU detection limits [25].

#### 4. Conclusions

In the present paper, chemical, microstructural, physical, and thermodynamic properties of BSTCo5 powder obtained in hydrothermal conditions were investigated. For a proper evaluation of potential applications as a sensing material in CO<sub>2</sub> detection, the composition and thermodynamic stability of the powder was first assessed at 800 and 1000 °C.

It was shown that BSTCo5 was stable at 1200 °C, according to DSC/TG analysis. BSTCo5, as an obtained nanopowder, consisted of a mixture of phases (cubic and tetragonal) at 1000 °C. It was likely that its cubic structure prevailed, which was also supported by Raman spectroscopy.

Thermal conductivity, thermal diffusivity, and specific heat were consistent with literature data for BaTiO<sub>3</sub> compounds, and the variation of data occurred due to the dopants used, as well as the different manufacturing procedures and different techniques used for thermal conductivity measurement. Further studies may aim at improving thermal conductivity properties using co-doping with mixed rare-earth oxides.

The BSTCo5 that was heat-treated at 800 °C, encoded BSTCo5\_800, presented high selectivity for CO<sub>2</sub> related to other potential interfering gases. This ability, together with the good signal, simple and low-cost technology, and the low power consumption corresponding to RT operation, suggested that BSTCo5\_800 had good development potential for portable CO<sub>2</sub> detectors. Two possible mechanisms of carbon dioxide (CO<sub>2</sub>) detection via electrical resistance modification were also proposed under real operating conditions.

**Author Contributions:** Conceptualization: R.M.P.; methodology: C.F.C., A.S. (Adelina Stanoiu); validation: C.F.C., C.E.S. and S.E.B.; investigation: C.N., I.A.T., A.M., D.V.D. and E.M.A.; data curation: E.M.A., O.G.F. and C.E.S.; writing—original draft preparation: C.F.C.; writing—review & editing: R.M.P., A.S. (Adelina Stanoiu) and S.E.B.; project administration: R.M.P. and A.S. (Arcadie Sobetkii); funding acquisition: R.M.P. and A.S. (Arcadie Sobetkii). All authors have read and agreed to the published version of the manuscript.

**Funding:** This work was carried out through the Core Program with the support of MCI, project no. 19 19 02 01 (contract no. 6N/2019) and project no. 19-03 (contract no. 21 N/2019). We gratefully acknowledge UEFISCDI for financial support under project 198/2012-SENSGAS and ERAMIN-ID 87 contract 50/2018 MONAMIX.

**Conflicts of Interest:** The authors declare no conflict of interest.

#### References

1. Feng, S.; Farha, F.; Li, Q.; Wan, Y.; Xu, Y.; Zhang, T.; Ning, H. Review on smart gas sensing technology. *Sensors* **2019**, *19*, 3760. [[CrossRef](#)]
2. Kobayashi, H.; Kobayashi, T. Heteroepitaxial growth of quaternary baxsr1–xtio3 thin films by arf excimer laser ablation. *Jpn. J. Appl. Phys.* **1994**, *33*, L533–L536. [[CrossRef](#)]
3. Tombak, A.; Maria, J.P.; Ayguavives, F.T.; Jin, Z.; Stauf, G.T.; Kingon, A.I.; Mortazawi, A. Voltage-controlled RF filters employing thin-film barium-strontium-titanate tunable capacitors. *IEEE Trans. Microw. Theory Tech.* **2003**, *51*, 462–467. [[CrossRef](#)]
4. Feng, Z.; Fathelbab, W.M.; Lam, P.G.; Haridasan, V.; Maria, J.P.; Kingon, A.I.; Steer, M.B. Narrowband Barium Strontium Titanate (BST) tunable bandpass filters at X-band. In Proceedings of the IEEE MTT-S International Microwave Symposium Digest, Boston, MA, USA, 7–12 June 2009; pp. 1061–1064.
5. Tariverdian, T.; Behnamghader, A.; Brouki Milan, P.; Barzegar-Bafrooei, H.; Mozafari, M. 3D-printed barium strontium titanate-based piezoelectric scaffolds for bone tissue engineering. *Ceram. Int.* **2019**, *45*, 14029–14038. [[CrossRef](#)]
6. Meyer, R.J.; Newnham, R.E.; Amin, A.; Kulwicki, B.M. Flexensional Barium Strontium Titanate Actuators. *J. Am. Ceram. Soc.* **2003**, *86*, 934–938. [[CrossRef](#)]
7. Bain, A.K.; Jackson, T.J.; Koutsonas, Y.; Cryan, M.; Yu, S.; Hill, M.; Varrazza, R.; Rorison, J.; Lancaster, M.J. Optical properties of barium strontium titanate(BST) Ferroelectric thin films. *Ferroelectr. Lett. Sect.* **2007**, *34*, 149–154. [[CrossRef](#)]
8. Puli, V.S.; Li, P.; Adireddy, S.; Chrisey, D.B. Crystal structure, dielectric, ferroelectric and energy storage properties of La-doped BaTiO<sub>3</sub> semiconducting ceramics. *J. Adv. Dielectr.* **2015**, *5*. [[CrossRef](#)]

9. Mahmood, W.; Yunus, M.; Ridha, N.J.; Halim, S.A.; Talib, Z.A.; Al-Asfoor, F.K.M.; Primus, W.C. Effect of Sr Substitution on Structure and Thermal Diffusivity of  $Ba_{1-x}Sr_xTiO_3$  Ceramic. *Am. J. Eng. Appl. Sci.* **2009**, *2*, 661–664.
10. Sadeghzadeh Attar, A.; Salehi Sichani, E.; Sharafi, S. Structural and dielectric properties of Bi-doped barium strontium titanate nanopowders synthesized by sol-gel method. *J. Mater. Res. Technol.* **2017**, *6*, 108–115. [[CrossRef](#)]
11. Zhang, T.; Ni, H. Pyroelectric and dielectric properties of sol-gel derived barium-strontium-titanate ( $Ba_{0.64}Sr_{0.36}TiO_3$ ) thin films. *Sens. Actuators A Phys.* **2002**, *100*, 252–256. [[CrossRef](#)]
12. Farahani, H.; Wagiran, R.; Yurchenko, O.; Urban, G.A. Barium Strontium Titanate Humidity Sensor: Impact of Doping on the Structural and Electrical Properties. *Proceedings* **2018**, *2*, 1007. [[CrossRef](#)]
13. Stanoiu, A.; Piticescu, R.M.; Simion, C.E.; Rusti-Ciobota, C.F.; Florea, O.G.; Teodorescu, V.S.; Osiceanu, P.; Sobetkii, A.; Badilita, V. H<sub>2</sub>S selective sensitivity of Cu doped BaSrTiO<sub>3</sub> under operando conditions and the associated sensing mechanism. *Sens. Actuators B Chem.* **2018**, *264*, 327–336. [[CrossRef](#)]
14. Kavitha, V.; Mayandi, J.; Mahalingam, P.; Sethupathi, N. Structural, optical and electrical studies on zinc doped barium strontium titanate as photo-anode for DSSC device. *Mater. Today Proc.* **2019**. [[CrossRef](#)]
15. Li, M.L.; Xu, M.X. Effect of dispersant on preparation of barium-strontium titanate powders through oxalate co-precipitation method. *Mater. Res. Bull.* **2009**, *44*, 937–942. [[CrossRef](#)]
16. Kharisov, B.I.; Kharissova, O.V.; Ortiz, U. Microwave Hydrothermal and Solvothermal Processing of Materials and Compounds. In *The Development and Application of Microwave Heating*; InTech: London, UK, 2012.
17. Chen, W.; Zhu, Q. Synthesis of barium strontium titanate nanorods in reverse microemulsion. *Mater. Lett.* **2007**, *61*, 3378–3380. [[CrossRef](#)]
18. Reshmi, R.; Asha, A.S.; Krishnaprasad, P.S.; Jayaraj, M.K.; Sebastian, M.T. High tunability of pulsed laser deposited  $Ba_{0.7}Sr_{0.3}TiO_3$  thin films on perovskite oxide electrode. *J. Alloys Compd.* **2011**, *509*, 6561–6566. [[CrossRef](#)]
19. Liu, C.; Liu, P. Microstructure and dielectric properties of BST ceramics derived from high-energy ball-milling. *J. Alloys Compd.* **2014**, *584*, 114–118. [[CrossRef](#)]
20. Razak, K.A.; Asadov, A.; Gao, W. Phase content and dielectrical properties of sintered BaSrTiO ceramics prepared by a high temperature hydrothermal technique. *Ceram. Int.* **2009**, *35*, 2781–2787. [[CrossRef](#)]
21. Rusti, C.F.; Badilita, V.; Sofronia, A.M.; Taloi, D.; Anghel, E.M.; Maxim, F.; Hornoiu, C.; Munteanu, C.; Piticescu, R.M.; Tanasescu, S. Thermodynamic properties of the  $Ba_{0.75}Sr_{0.25}TiO_3$  nanopowders obtained by hydrothermal synthesis. *J. Alloys Compd.* **2017**, *693*, 1000–1010. [[CrossRef](#)]
22. Sasirekha, N.; Rajesh, B.; Chen, Y.W. Hydrothermal synthesis of barium titanate: Effect of titania precursor and calcination temperature on phase transition. *Ind. Eng. Chem. Res.* **2008**, *47*, 1868–1875. [[CrossRef](#)]
23. Mi, G.; Horvath, C.; Aktary, M.; Van, V. Silicon microring refractometric sensor for atmospheric CO<sub>2</sub> gas monitoring. *Opt. Express* **2016**, *24*, 1773. [[CrossRef](#)]
24. Scholz, L.; Ortiz Perez, A.; Bierer, B.; Wöllenstein, J.; Palzer, S. Gas sensors for climate research. *J. Sens. Sens. Syst.* **2018**, *7*, 535–541. [[CrossRef](#)]
25. Satyanarayana, L.; Noh, W.S.; Lee, W.Y.; Jin, G.H.; Park, J.S. A high temperature potentiometric CO<sub>2</sub> sensor mixed with binary carbonate and glassy ceramic oxide. *Mater. Chem. Phys.* **2009**, *114*, 827–831. [[CrossRef](#)]
26. Pandey, S.K.; Kim, K.-H. The Relative Performance of NDIR-based Sensors in the Near Real-time Analysis of CO<sub>2</sub> in Air. *Sensors* **2007**, *7*, 1683–1696. [[CrossRef](#)] [[PubMed](#)]
27. Matsubara, S.; Kaneko, S.; Morimoto, S.; Shimizu, S.; Ishihara, T.; Takita, Y. Practical capacitive type CO<sub>2</sub> sensor using CeO<sub>2</sub>/BaCO<sub>3</sub>/CuO ceramics. *Sens. Actuators B Chem.* **2000**, *65*, 128–132. [[CrossRef](#)]
28. Chen, Y.; Wang, D.; Qin, H.; Zhang, H.; Zhang, Z.; Zhou, G.; Gao, C.; Hu, J. CO<sub>2</sub> sensing properties and mechanism of PrFeO<sub>3</sub> and NdFeO<sub>3</sub> thick film sensor. *J. Rare Earths* **2019**, *37*, 80–87. [[CrossRef](#)]
29. Ghosh, A.; Zhang, C.; Shi, S.; Zhang, H. High temperature CO<sub>2</sub> sensing and its cross-sensitivity towards H<sub>2</sub> and CO gas using calcium doped ZnO thin film coated langasite SAW sensor. *Sens. Actuators B Chem.* **2019**, *301*, 126958. [[CrossRef](#)]
30. Motoc, A.M.; Valsan, S.; Slobozeanu, A.E.; Corban, M.; Valerini, D.; Prakasam, M.; Botan, M.; Dragut, V.; Vasile, B.S.; Surdu, A.V.; et al. Design, Fabrication, and Characterization of New Materials Based on Zirconia Doped with Mixed Rare Earth Oxides: Review and First Experimental Results. *Metals (Basel)* **2020**, *10*, 746. [[CrossRef](#)]

31. Sobetkii, A.; Vişan, M.; Piticescu, R.M.; Ciobota (Ruşti), C.F.; Motoc, A.M.; Ionică, M.; Ulieru, D. Cu Doped BST Thin Films Deposition Process by RF-Sputtering Method. Patent No. 131119, 30 July 2019.
32. Stanoiu, A.; Simion, C.E.; Calderon-Moreno, J.M.; Osiceanu, P.; Florea, M.; Teodorescu, V.S.; Somacescu, S. Sensors based on mesoporous SnO<sub>2</sub>-CuWO<sub>4</sub> with high selective sensitivity to H<sub>2</sub>S at low operating temperature. *J. Hazard. Mater.* **2017**, *331*, 150–160. [[CrossRef](#)]
33. Jartych, E.; Pikula, T.; Garbarz-Glos, B.; Panek, R. Mössbauer Spectroscopy Studies of Fe-Doped BaTiO<sub>3</sub> Ceramics. *Acta Phys. Pol. A* **2018**, *134*, 1058–1062. [[CrossRef](#)]
34. Vinnik, D.A.; Trofimov, E.A.; Zhivulin, V.E.; Gudkova, S.A.; Zaitseva, O.V.; Zherebtsov, D.A.; Starikov, A.Y.; Sherstyuk, D.P.; Amirov, A.A.; Kalgin, A.V.; et al. High Entropy Oxide Phases with Perovskite Structure. *Nanomaterials* **2020**, *10*, 268. [[CrossRef](#)] [[PubMed](#)]
35. Bomlai, P.; Sirikulrat, N.; Brown, A.; Milne, S.J. Effects of TiO<sub>2</sub> and SiO<sub>2</sub> additions on phase formation, microstructures and PTCR characteristics of Sb-doped barium strontium titanate ceramics. *J. Eur. Ceram. Soc.* **2005**, *25*, 1905–1918. [[CrossRef](#)]
36. Didomenico, M.; Wemple, S.H.; Porto, S.P.S.; Bauman, R.P. Raman spectrum of single-domain BaTiO<sub>3</sub>. *Phys. Rev.* **1968**, *174*, 522–530. [[CrossRef](#)]
37. Smith, M.B.; Page, K.; Siegrist, T.; Redmond, P.L.; Walter, E.C.; Seshadri, R.; Brus, L.E.; Steigerwald, M.L. Crystal structure and the paraelectric-to-ferroelectric phase transition of nanoscale BaTiO<sub>3</sub>. *J. Am. Chem. Soc.* **2008**, *130*, 6955–6963. [[CrossRef](#)]
38. Slodczyk, A.; Colomban, P. Probing the Nanodomain Origin and Phase Transition Mechanisms in (Un)Poled PMN-PT Single Crystals and Textured Ceramics. *Materials* **2010**, *3*, 5007–5028. [[CrossRef](#)] [[PubMed](#)]
39. Tenne, D.A.; Xi, X. Raman Spectroscopy of Ferroelectric Thin Films and Superlattices. *J. Am. Ceram. Soc.* **2008**, *91*, 1820–1834. [[CrossRef](#)]
40. Zribi, O.; Garbovskiy, Y.; Glushchenko, A. Single-step colloidal processing of stable aqueous dispersions of ferroelectric nanoparticles for biomedical imaging. *Mater. Res. Express* **2015**, *1*, 045401. [[CrossRef](#)]
41. Simões, A.Z.; Moura, F.; Onofre, T.B.; Ramirez, M.A.; Varela, J.A.; Longo, E. Microwave-hydrothermal synthesis of barium strontium titanate nanoparticles. *J. Alloys Compd.* **2010**, *508*, 620–624. [[CrossRef](#)]
42. Rout, S.K.; Panigrahi, S. Mechanism of phase formation of BaTiO<sub>3</sub>-SrTiO<sub>3</sub> solid solution through solid—Oxide reaction. *Indian J. Pure Appl. Phys.* **2006**, *44*, 606–611.
43. He, Y. Heat capacity, thermal conductivity, and thermal expansion of barium titanate-based ceramics. *Thermochim. Acta* **2004**, *419*, 135–141. [[CrossRef](#)]
44. Shirane, G.; Takeda, A. Transition. Energy and Volume Change at Three Transitions in Barium Titanate. *J. Phys. Soc. Jpn.* **1952**, *7*, 1–4. [[CrossRef](#)]
45. Popescu, G.; Moldovan, P.; Bejan, S.; Miculescu, M.; Miculescu, F. Thermophysical properties and microstructural analysis of AZ80 magnesium alloys designed for automotive industry. In Proceedings of the Materials Science and Technology Conference and Exhibition, MS and T'08, Pittsburgh, PA, USA, 5–9 October 2008.
46. Gas Sensing Performance of Pure and Modified BST Thick Film Resistor. Available online: [https://www.researchgate.net/publication/291160745\\_Gas\\_Sensing\\_Performance\\_of\\_Pure\\_and\\_Modified\\_BST\\_Thick\\_Film\\_Resistor](https://www.researchgate.net/publication/291160745_Gas_Sensing_Performance_of_Pure_and_Modified_BST_Thick_Film_Resistor) (accessed on 8 October 2020).
47. Sediments, Diagenesis, and Sedimentary Rocks, 1st ed. Available online: <https://www.elsevier.com/books/sediments-diagenesis-and-sedimentary-rocks/mackenzie/978-0-08-044849-7> (accessed on 22 September 2020).
48. Chen, Z.; Concepcion, J.J.; Brennaman, M.K.; Kang, P.; Norris, M.R.; Hoertz, P.G.; Meyer, T.J. Splitting CO<sub>2</sub> into CO and O<sub>2</sub> by a single catalyst. *Proc. Natl. Acad. Sci. USA* **2012**, *109*, 15606–15611. [[CrossRef](#)] [[PubMed](#)]

**Publisher's Note:** MDPI stays neutral with regard to jurisdictional claims in published maps and institutional affiliations.



© 2020 by the authors. Licensee MDPI, Basel, Switzerland. This article is an open access article distributed under the terms and conditions of the Creative Commons Attribution (CC BY) license (<http://creativecommons.org/licenses/by/4.0/>).